

REGULAR PAPER

Low turn-on voltage and high breakdown GaN Schottky barrier diodes for RF energy harvesting applications

To cite this article: Haoran Wang *et al* 2020 *Jpn. J. Appl. Phys.* **59** SGGD12

View the [article online](#) for updates and enhancements.



Low turn-on voltage and high breakdown GaN Schottky barrier diodes for RF energy harvesting applications

Haoran Wang^{1*}, Chung-Hsin Li¹, Yeke Liu¹, Sumin D. Joseph², Yi Huang^{2*}, and Shawn S. H. Hsu¹

¹Institute of Electronics Engineering, NTHU, Hsinchu 30013, Taiwan

²Dept. of EEE, University of Liverpool, Liverpool L69 3GJ, United Kingdom

*E-mail: s105022467@m105.nthu.edu.tw; Yi.Huang@liverpool.ac.uk

Received October 2, 2019; revised December 29, 2019; accepted January 21, 2020; published online February 28, 2020

This work presents the design, fabrication, and analysis of GaN Schottky barrier diodes with multi-finger structure on the silicon substrate using various layout parameters, aiming for RF energy harvesting applications. The measured results demonstrate a low turn-on voltage (V_{on}) and a high breakdown voltage (V_{BK}) of 0.56 V and 47 V, respectively. A high cut-off frequency (f_c) of 360.9 GHz under reverse bias of -10 V is also obtained for a two-finger device with each finger of $W = 12.5 \mu\text{m}$ and $L = 0.2 \mu\text{m}$. © 2020 The Japan Society of Applied Physics

1. Introduction

The trend of the Internet of Things predicts there will be more than 50 billion devices connected in 2020, including many sensors for various applications. One major issue for these sensors is the power supply.^{1,2)} Using batteries may not be a good solution since these sensors could be deployed in various locations and replacement of the batteries becomes very inefficient. RF energy harvesting provides an attractive solution, where the ambient EM signals generated by different RF sources such as the cellphone base stations and WiFi routers could be captured by the antenna.^{3–5)} An energy harvesting system using matching circuits for the antenna along with a rectifier can generate energy from the wireless signals to charge the sensors or other mobile devices.^{6,7)} The Schottky barrier diode (SBD) is an essential component for converting the RF energy to DC power. Since the received RF power will be relatively low and the frequency is high,^{8,9)} the diodes with low turn-on voltage (V_{on}), low on-resistance (R_{ON}) and high operating frequency are important to enhance the conversion efficiency.¹⁰⁾ Also, a high breakdown voltage of the diode is preferred to improve the system robustness, since a very high EM energy could be encountered on some occasions.^{4,11)}

As a wide bandgap material, GaN has a large breakdown field with a much higher saturation electron velocity compared with other conventional semiconductor materials such as silicon and GaAs. With fundamental material advantages, GaN-based devices are very suitable for high power and high-speed applications.^{12–15)} Recent progress also reported high-quality GaN epitaxial layers grown on large-scale silicon substrates, making low cost and high performance GaN SBDs possible.^{16–18)} As a result, the GaN-based SBD is an excellent candidate for RF energy harvesting applications.¹⁹⁾ Compared with the GaAs SBDs, the reported cut-off frequency (f_c) of GaN SBDs is relatively lower,²⁰⁾ which indicates that it is crucial to optimize the device design such as the parasitic series resistance (R_s), including contact resistance (R_c), cathode resistance ($R_{cathode}$), anode resistance (R_{Anode}), and the resistance between anode and cathode (R_{AC}).²¹⁾ Also, the junction capacitance (C_j) which is related to the doping profile of the epitaxial layer²²⁾ and the capacitance between two electrodes (C_{AC}) are the important parameters to improve the device performance.

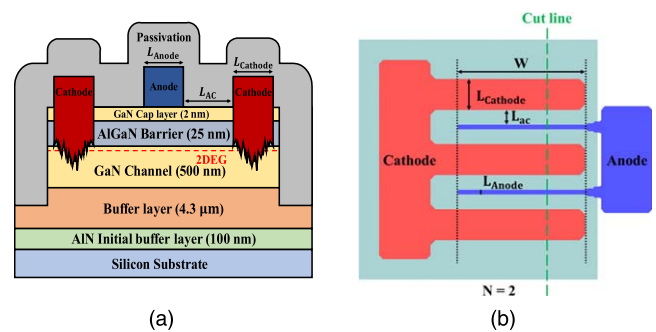


Fig. 1. (Color online) Device (a) cross-section and (b) layout.

In this paper, we demonstrate high frequency multi-finger AlGaIn/GaN SBDs on the silicon substrate. Devices with different layout geometries are designed, fabricated, and analyzed for both DC and RF characteristics. In addition, small-signal model parameters are extracted from the measured S-parameters for details analysis.²³⁾ In addition, the simulated S-parameters based on the model are compared with the measured results. The preliminary results have been shown at the 2019 SSDM, and this paper further elaborates the details of device fabrication and analysis.

2. Experimental methods

Figure 1 shows the epitaxial layer structure of the AlGaIn/GaN SBDs grown by metal-organic chemical vapor deposition (MOCVD) on a silicon substrate. The epitaxial layers consist of a 100 nm AlN initial buffer layer, 4.3 μm carbon-doped GaN buffer, 500 nm GaN channel layer, 25 nm Al_{0.25}Ga_{0.75}N barrier, and a 2 nm UID GaN cap layer, as shown in Fig. 1(a).

Fabrication of the device began with mesa isolation, which was done by a reactive ion etching (RIE) system with a Cl₂/BCl₃ mixture gas for an etching depth of ~ 150 nm. For the formation of the cathode, Ti/Al/Ni/Au Ohmic metal was deposited using a thermal evaporation system followed by rapid thermal annealing at 850 °C for 30 s in the N₂ ambient, which results in a low contact resistance.^{24,25)} The anode with Ti/Au stack layers was then developed by e-beam lithography to improve the RF performance. After e-beam lithography, the Schottky metal stack of Ti/Au was deposited by thermal evaporation and followed by a lift-off process.

Due to the low metal work function of Ti/Au metal stack, the turn-on voltage of the device can be reduced, while V_{BK} may be degraded. It should be mentioned that Ti is used as the Schottky metal instead of the typically used Ni for a low turn-on voltage,²⁶⁾ which is beneficial for energy harvest applications. The RF pads with a metal stack of Ni/Au was deposited using thermal evaporation to allow on-wafer measurements, which are suitable for ground–signal–ground (GSG) probes.

Different layout geometries are designed to investigate the tradeoff and find out the optimal solution regarding parasitic resistance, cut-off frequency, and breakdown voltage. Finally, device passivation with multilayer structure of $\text{SiN}_x/\text{SiO}_2/\text{SiN}_x$ was deposited by a PECVD system at 300 °C. Note that the finger type layout is adopted, which can be defined by W (finger width), L_{Anode} (finger length of anode), L_{Cathode} (finger length of cathode), L_{AC} (distance between anode and cathode), and N (anode finger number). Figure 1(b) shows an example of a two-finger SBD. A contact resistance R_c of 0.5 $\Omega\cdot\text{mm}$ and a sheet resistance R_{sh} of 413 Ω/\square were obtained, respectively, by the transmission line method (TLM) after passivation. Figure 2 shows the overall device structure by optical microscope with layout parameters $L_{\text{AC}} = 2 \mu\text{m}$, $L_{\text{Anode}} = 0.2 \mu\text{m}$, and $W = 12.5 \mu\text{m}$.

3. Device modeling

For in-depth analysis of the proposed AlGaN/GaN SBDs, we establish a high frequency diode equivalent circuit small-signal model, according to the layout and device structure characteristic as illustrated in Fig. 3(a). With the high resistivity silicon substrate ($\rho = 6000 \Omega\cdot\text{cm}$), the parasitic substrate capacitance (C_{sub}) and resistance (R_{sub}), which appears in Fig. 3(a), are neglected for simplicity as shown in Fig. 3(b). Considering the effect of bias voltage, a simplified large-signal model is also established as shown in Fig. 3(c), where L_s and R_s are the parasitic series inductance and resistance, C_j and R_j represent the junction capacitance and resistance, L_{pad} and C_{pad} are the parasitic effects of RF pads. The pad capacitance (C_{pad}) can be extracted as 24fF at 50 GHz. Based on the measured S-parameters of SBD under different bias conditions, the open-short de-embedding procedure is performed first by the Y - and Z - parameters of the testkeys to obtain the intrinsic device characteristics.²⁷⁾ The bias-dependent R_s can then be extracted using the simplified small-signal model as shown in Fig. 3(b). At high frequencies, C_j becomes a short circuit, the real part of Z_{int} can be

approximated as R_s . The value of L_s is 90 pH, which can also be obtained simultaneously.

After the extraction of small-signal model parameters, the cut-off frequency (f_c) of the device can be expressed by R_s and C_j .²⁸⁾ Since R_s and C_j are under the influence of DC bias, R_s and C_j turn into voltage-dependent parameters $R_s(V)$ and $C_j(V)$ in the large-signal model. Similarly, the small-signal parameter R_j [see Fig. 3(b)] becomes a voltage-dependent current source i_D described by the equation shown below, where I_D and i_d represent DC and AC current, respectively, and V_D is the bias voltage including DC and AC bias. Note that the thermal resistance R_{th} (V) is also considered in this model, which is also related to the bias voltage.

$$i_D = I_D + i_d = I_s e^{\frac{q(V_D - i_D R_s)}{n k T}} \quad (1)$$

4. Measured results and discussion

4.1. DC characteristics

To analyze the performance dependence of the device layout, the SBDs on the silicon substrate are designed with various layout parameters of L_{AC} , L_{Anode} , W , and N . Note that L_{Cathode} of the device is fixed at 6 μm for a better device yield. Figure 4(a) shows the measured results of a two-finger SBD ($W = 12.5 \mu\text{m}$ and $L_{\text{Cathode}} = 6 \mu\text{m}$) with two different L_{AC} of 2 and 3 μm . The forward current densities of 90 and 77 mA mm^{-2} can be achieved, respectively. Also, V_{on} of 0.56 and 0.63 V, V_{BK} of 37 and 47 V are obtained for devices with L_{AC} of 2 and 3 μm , respectively, as shown in Fig. 4(b).

It was found that tradeoffs exist among forward current, V_{on} and V_{BK} regarding the anode–cathode distance. As L_{AC} reduces, the parasitic access resistance becomes smaller, resulting in improvement of V_{on} and current density (I_D). However, V_{BK} is also degraded due to the smaller distance between the two electrodes. Figure 5 presents the dependence of V_{on} and V_{BK} on the finger length L_{Anode} . As can be seen, the current density increases with the finger length [Fig. 5(a)]. The increased current density can be attributed to the reduced parasitic anode resistance with an increased L_{Anode} . A highest current density of 130 mA mm^{-2} can be obtained for $L_{\text{Anode}} = 0.8 \mu\text{m}$. On the other hand, the impact of L_{Anode} is not obvious on V_{BK} as shown in Fig. 5(b). Changing of W and N has a similar effect on the SBD characteristic. As the size reduces, the current density increases and V_{on} reduces, as shown in Figs. 6(a) and 6(c). This could be attributed to the

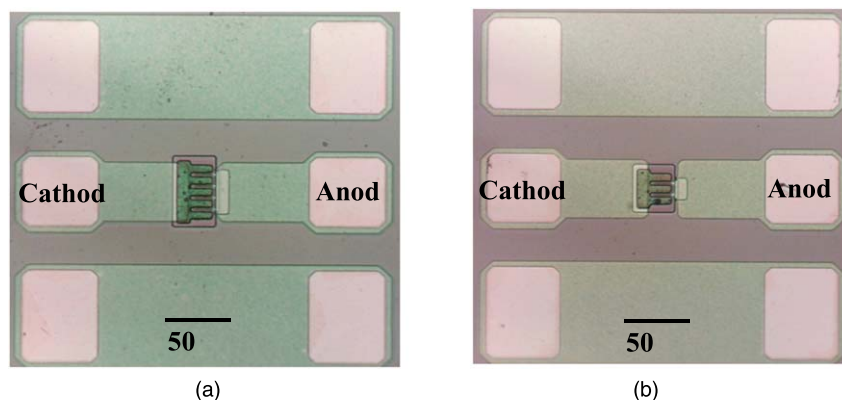


Fig. 2. (Color online) Micro graphs of fabricated SBDs with (a) $N = 2$ (b) $N = 4$.

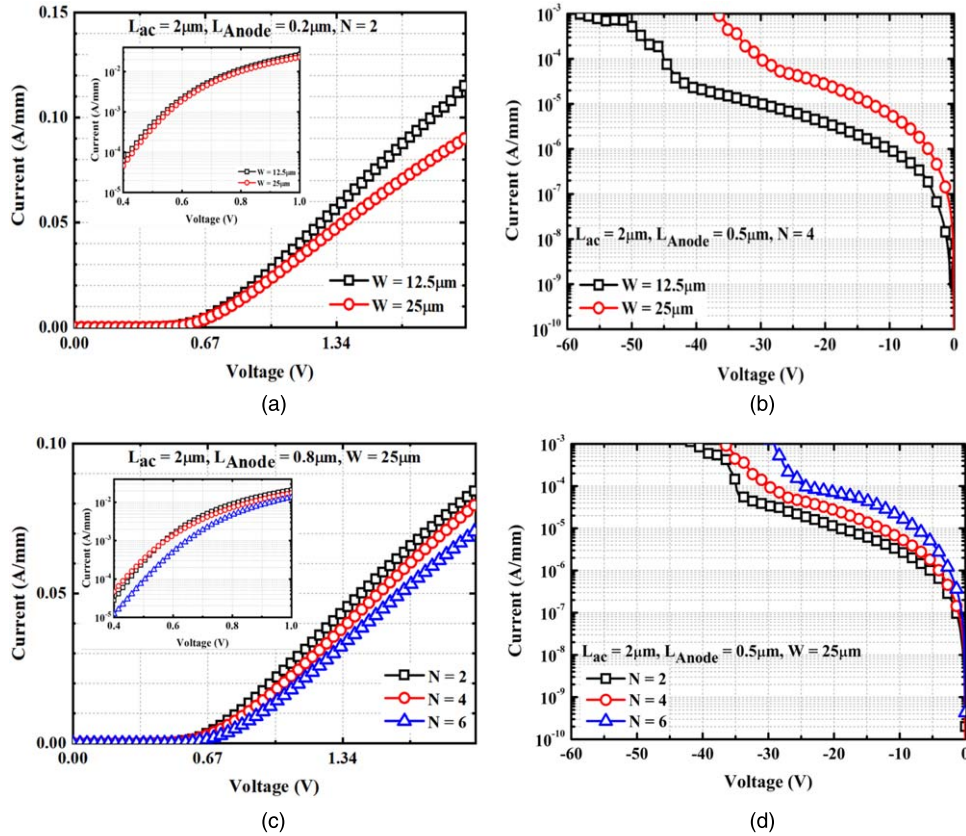


Fig. 6. (Color online) I - V characteristic with various W and N .

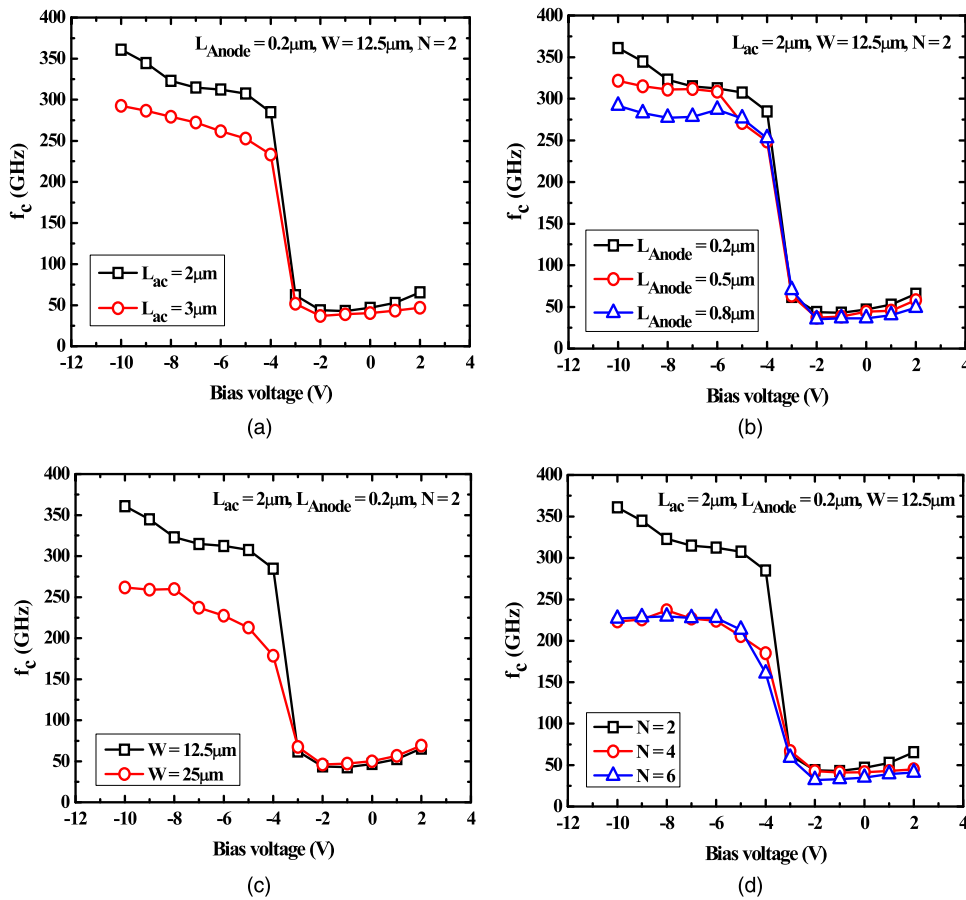


Fig. 7. (Color online) Extracted values of f_c with variable layout parameters.

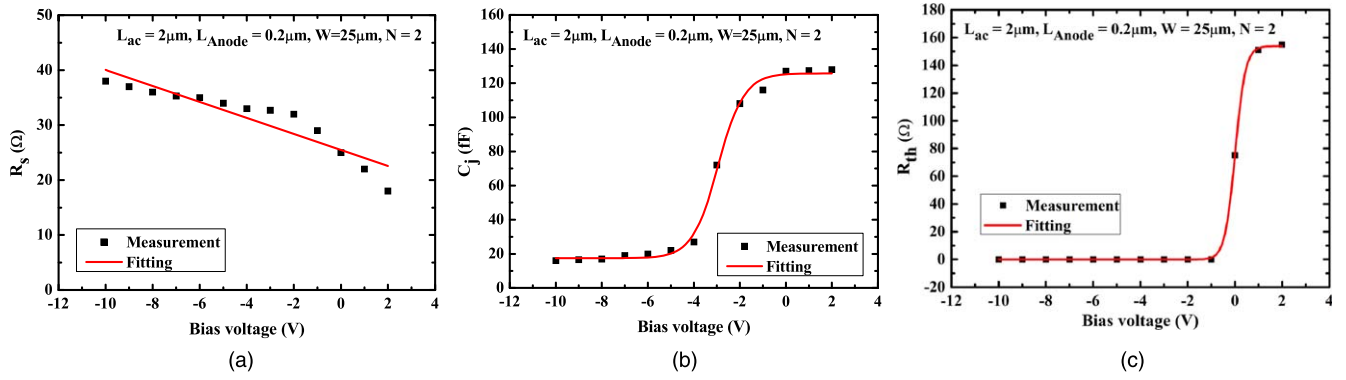


Fig. 8. (Color online) Bias-dependent elements of large-signal model (a) R_s (b) C_j (c) R_{th} .

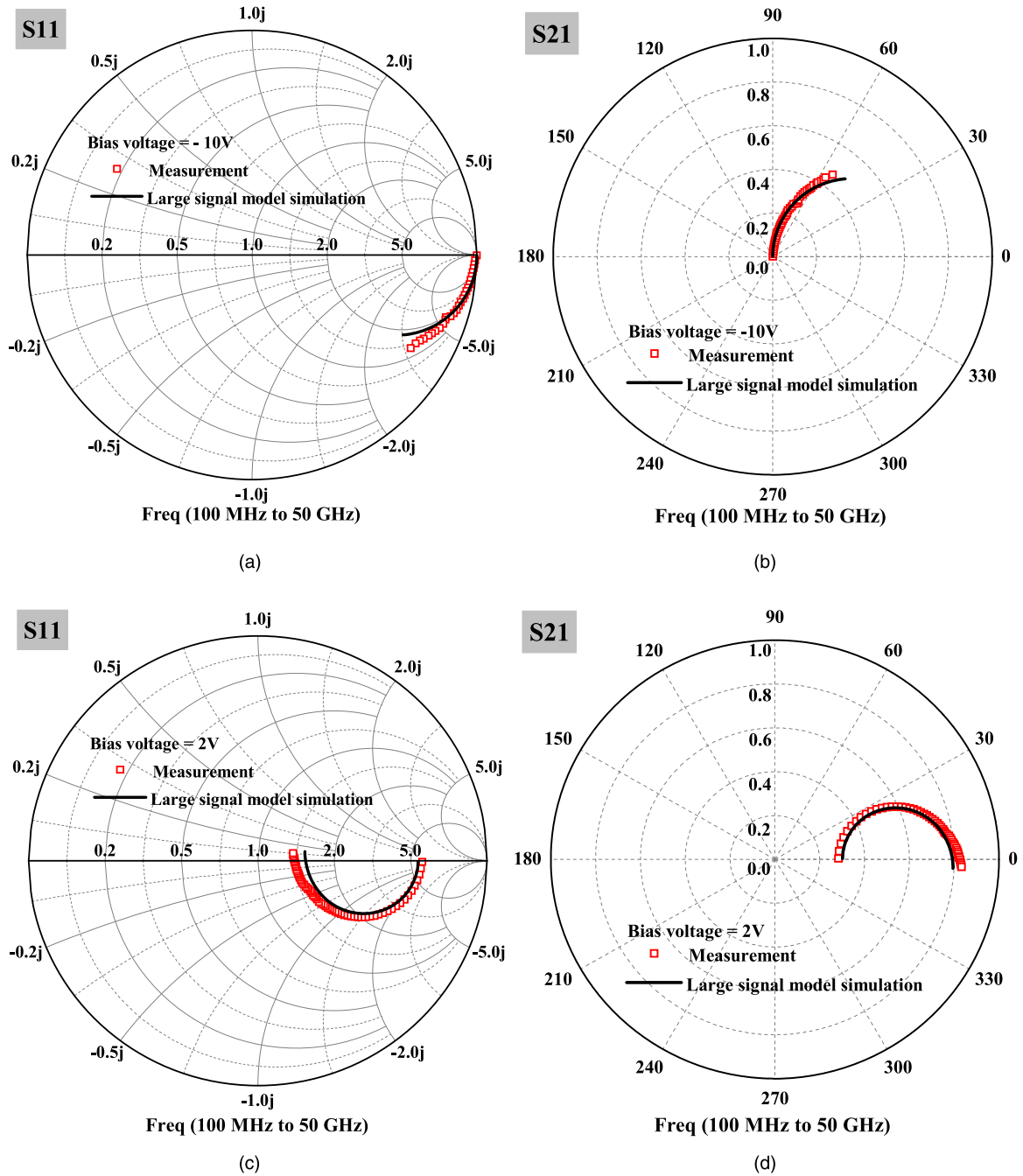


Fig. 9. (Color online) S-parameters comparison between simulation and measurement results (a) S_{11} under bias voltage = -10 V, (b) S_{21} under bias voltage = -10 V, (c) S_{11} under bias voltage = 2 V, and (d) S_{21} under bias voltage = 2 V.

based on the large-signal model. A very good agreement can be obtained as shown in Fig. 9.

$$R_S = mv_D + b \quad (2)$$

$$R_{th}, C_j = A_1 + \frac{A_1 - A_2}{1 + e^{(v_D - x_0)/\tau}} \quad (3)$$

5. Conclusions

Aiming for RF energy harvesting applications, GaN Schottky barrier diodes with low turn-on voltage and high breakdown voltage were designed and fabricated in this work. SBDs with different layout parameters L_{AC} , L_{Anode} , W and N are fabricated to investigate the dependence between device layout parameters and characteristics and to find optimal layout geometry for the desired applications. A low V_{on} and a high V_{BK} of 0.56 V and 47 V, respectively, were demonstrated. A high cut-off frequency of 360.9 GHz was also obtained for a two-finger device with each finger of $W = 12.5 \mu\text{m}$, $L_{AC} = 2 \mu\text{m}$ and $L_{Anode} = 0.2 \mu\text{m}$. The analysis based on the extracted small-signal model also provides more insight into the obtained results. The large-signal model was established by analyzing the behavior of R_S , C_j and R_{th} , where the simulation results showed a good agreement with the measurements.

ORCID iDs

Yeke Liu  <https://orcid.org/0000-0003-3774-3871>

- 1) S. Tozlu, M. Senel, W. Mao, and A. Keshavarzian, *IEEE Commun. Mag.* **50**, 134 (2012).
- 2) L. Atzori, A. Iera, and G. Morabito, *Comput. Networks.* **54**, 2787 (2010).
- 3) S.-Y. Lee, Z.-X. Liao, and C.-H. Lee, *IEEE Trans. Very Large Scale Integr. Syst.* (2019).
- 4) D. W. Bouler, J. Baxter, and D. Costinett, , 2016IEEE PELS Workshop on Emerging Technologies: Wireless Power Transfer, 2016, p. 231.
- 5) X. Lu, P. Wang, D. Niyato, D. I. Kim, and Z. Han, *IEEE Commun. Surv. Tutorials* **17**, 757 (2014).
- 6) C. Song, Y. Huang, P. Carter, J. Zhou, S. Yuan, Q. Xu, and M. Kod, *IEEE Trans. Antennas Propag.* **64**, 3160 (2016).
- 7) C. Song, Y. Huang, J. Zhou, J. Zhang, S. Yuan, and P. Carter, *IEEE Trans. Antennas Propag.* **63**, 3486 (2015).
- 8) Y. Lian, Y. Lin, J. Yang, C. Cheng, and S. S. H. Hsu, *IEEE Electron Device Lett.* **34**, 981 (2013).
- 9) S. S. H. Hsu, C. Tsou, Y. Lian, and Y. Lin, *IEEE Int. Symp. Radio-Frequency Integration Technology*, 2016, p. 1.
- 10) S. Han, S. Yang, R. Li, X. Wu, and K. Sheng, *IEEE Trans. Power Electron.* **34**, 5012 (2018).
- 11) I. Kizilyalli, E. Carlson, and D. Cunningham, *IEEE Int. Electron Devices Meet.*, 2018, p.19.6. 1.
- 12) X. Zhang, X. Zou, X. Lu, C. W. Tang, and K. M. Lau, *IEEE Trans. Electron Devices* **64**, 809 (2017).
- 13) M. P. King, A. Armstrong, J. R. Dickerson, G. Vizkelethy, R. M. Fleming, J. Campbell, W. R. Wampler, I. Kizilyalli, D. Bour, and O. Aktas, *IEEE Trans. Nucl. Sci.* **62**, 2912 (2015).
- 14) O. Ambacher, *J. Phys. D: Appl. Phys.* **31**, 2653 (1998).
- 15) E. O. Johnson, *RCA Rev.* **26**, 163 (1965).
- 16) T. Sugahara, J.-S. Lee, and K. Ohtsuka, *Jpn. J. Appl. Phys.* **43**, L1595 (2004).
- 17) A. Ubukata, K. Ikenaga, N. Akutsu, A. Yamaguchi, K. Matsumoto, T. Yamazaki, and T. Egawa, *J. Cryst. Growth* **298**, 198 (2007).
- 18) J. Hu, S. Stoffels, S. Lenci, G. Groeseneken, and S. Decoutere, *IEEE Electron Device Lett.* **37**, 310 (2016).
- 19) S. Kawasaki, R. Kishikawa, Y. Furuse, T. Nakaoka, S. Yoshida, K. Nishikawa, and H. Seita, *IEEE Int. Symp. Radio-Frequency Integration Technology*, 2017, p. 147.
- 20) N. Alijabbari, M. F. Bauwens, and R. M. Weikle, *IEEE Trans. Terahertz Sci. and Technol.* **5**, 73 (2015).
- 21) L. Efthymiou, G. Longobardi, G. Camuso, A. P. Hsieh, and F. Udrea, *Int. Semiconductor Conf.*, 2015, p. 211.
- 22) C. Jin, D. Pavlidis, and L. Considine, *The 5th European Microwave Integrated Circuits Conf.*, 2010, p. 118.
- 23) J. Ghosh and S. Ganguly, *Jpn. J. Appl. Phys.* **57**, 080305 (2018).
- 24) A. Motayed, R. Bathe, M. C. Wood, O. S. Diouf, R. D. Vispute, and S. N. Mohammad, *J. Appl. Phys.* **93**, 1087 (2003).
- 25) H.-G. Jang, J. Na, J.-J. Kim, Y.-R. Park, H.-S. Lee, D.-Y. Jung, J.-K. Mun, S. C. Ko, and E. S. Nam, *Jpn. J. Appl. Phys.* **54**, 070302 (2015).
- 26) C.-W. Tsou, K.-P. Wei, Y.-W. Lian, and S. S. H. Hsu, *IEEE Electron Device Lett.* **37**, 70 (2016).
- 27) T. Hirano, K. Okada, J. Hirokawa, and M. Ando, *Asia-Pacific Microwave Conf.*, 2010, p. 1436.
- 28) J. Semple, D. G. Georgiadou, G. Wyatt-Moon, G. Gelinck, and T. D. Anthopoulos, *Semicond. Sci. Technol.* **32**, 123002 (2017).
- 29) T. Kiuru, J. Mallat, A. V. Raisenen, and T. Narhi, *IEEE Trans. Microwave Theory Tech.* **59**, 2108 (2011).